Monte Carlo studies of D^{*-} production and semi-leptonic decay

G.V. Ybeles Smit

May 2003

Master thesis

VU/NIKHEF
HERMES group

Physics is like sex: Sure it may give some practical results,
but that's not why we do it

Richard P. Feynman

Summary

Photon-gluon fusion (PGF) processes are an important source of information about the polarisation of the gluons inside the nucleon. In the HERMES experiment at DESY charmed mesons are produced almost exclusively through PGF in deep-inelastic collisions of polarised electrons with a polarised nucleon target. The charged $D^{*\pm}$ mesons mainly decay into a (anti)D^0 meson and a pion, with subsequent decay of the (anti) D^0 meson into various combinations of kaons and pions.This study is devoted to the semileptonic decay $D^{*-} \rightarrow \overline{D^0}\ \pi^- \rightarrow K^+\ e^-\ \bar{\nu}_e\ \pi^-$. Using the results of Monte Carlo calculations performed with AROMA (production of charmed hadrons) and PYTHIA (other processes) domains in the kinematic variables and reconstructed masses are determined for which the ratio of events from D^{*-} decay and events from other processes is maximal using the ΔM method. This information will be used in the data analysis to obtain samples for extraction of the gluon polarisation. An optimisation of the ratio is found to be 3.5 with a loss of 65% of events in the events from $D^{*-} \rightarrow \overline{D^0}\ \pi^-$.

Contents

Introduction

The HERMES experiment at the German accelerator center DESY is involved with measuring the spin of the nucleon. The idea of spin arose at the beginning of the previous century, when observed atomic spectra did not fit the standard theory of that time. The so-called anomalous Zeeman effect was explained by postulating a fourth[1] quantum number called spin, m_s. By assuming that this number can have two values, the 'anomalous' spectra could be explained. G. Uhlenbeck postulated that this extra degree of freedom must be related to an intrinsic angular momentum of the electron [1]. When the hyperfine structure was discovered in 1947 by W. Lamb and R. Retherford, the spin formalism could be extended to nucleons.

In nuclear scattering experiments in the 1950's a large number of 'elementary' particles were observed. In 1961 M. Gell-Mann used a *symmetry group* that would classify the differences and similarities of the particles. He called it *'The eightfold way'*, because of the many occurrences of particle octets with related quantum numbers. The eightfold way led to the postulation of hadron constituents, called *quarks*.

Deep-inelastic scattering (DIS) experiments in the 1960's showed that the nucleons possess a substructure and are built up of *partons*. J. Bjorken and R. Feynman developed the parton model in 1968, and explained so-called *scaling* behaviour of the structure functions. Scaling means that at high four-momentum transfer the scattering process can be described as the absorption of the virtual photon by a free parton. Furthermore it was observed that the partons carry about $\frac{1}{3}$ of the total momentum of the nucleon. This can be explained by assuming that one is scattering on three point-like particles inside the nucleon, which are identified as the quarks of Gell-Mann. Later it showed that scaling is only an approximate property, and violations were

---

[1] Next to the *principal quantum number,* n, *orbital angular momentum q.n.,* l and *magnetic q.n.,* m_l

found in the scaling of the structure functions[2]. This called for the need of a *dynamical* quark model.

Due to the existence of a particle called the Δ^{++}, which is made of three up quarks with total spin $\frac{1}{2}$, a new quantum number was postulated to save the Pauli exclusion principle. This new degree of freedom was named colour and comes in six values: R, G, B and the *anti-colours*, $\overline{R}, \overline{G}, \overline{B}$. Together with the dynamical quark model, the colour property introduced a new gauge theory, quantum chromodynamics or QCD. This theory of strong nuclear interactions claimed the existence of mediating vector bosons, the quanta of the colour field, *gluons*. Direct evidence of the gluon was observed at DESY in 1979.

Results from experiments in which polarised energetic muons were inelastically scattered off polarised nucleons (EMC [2]), showed that only 20% of the spin of the proton could be accounted for by the spin of the valence quarks. These observations were confirmed in subsequent experiments (*e.g.* SMC at CERN, E142 at SLAC and later on HERMES at DESY). The spin of the nucleon can be written as the sum of three parts: $\frac{1}{2} = \frac{1}{2}\Delta\Sigma + \Delta g + L_z$. Here $\frac{1}{2}\Delta\Sigma$ represents the quark spin contribution, Δg is the gluon spin contribution and L_z is the orbital angular momentum of the partons. The observation that the valence quarks can account for only a small fraction of the nucleon spin, implies large contributions from the gluons and orbital momenta.

The contribution of the gluon spin can be determined in studies of photon-gluon fusion. Photon-gluon fusion is assumed to be the main process in which heavy quark anti-quark pairs are created. Because the photon-gluon fusion amplitude is dependent on the gluon-quark coupling, one may extract information about the gluons from these experiments. The reaction amplitude is dependent on the relative polarisation of the scattered particles, and by measuring asymmetries it is possible to determine the gluon polarisation Δg.

The heaviest quarks produced at HERMES are charm quarks, created mainly via photon-gluon fusion. In this thesis, attention will be focused on the charmed D^{*-} meson. One cannot measure these hadrons directly as they decay before they enter the detector. Therefore it is necessary to study the decays of these particles. Hence, experimentally one wishes ‘clean’ decay channels where a clear signal can be identified. The D mesons decay via hadronic processes as well as via semi-leptonic processes. An interesting semi-leptonic decay mode of the $\overline{D^0}$ meson is the decay into K^+, e^-, $\overline{\nu_e}$.

---

[2] This happens at low partonic momenta (low x)

The abundance of electrons is relatively small, and electrons can easily identified among the positrons of the HERA beam. Unfortunately the neutrino, interacting only via the weak force, is not detectable. So the benefits of the clean signal are suppressed by the partial reconstruction of events.

Monte Carlo simulations are crucial to give information on the kinematical variables of the particles and their decay products. This information is needed to select particles which originate from D^{*-} decay in the data. This thesis deals with production and analysis of Monte Carlo data of D^{*-} and it's semi-leptonic decay. It is divided into five chapters and an appendix. In the first chapter theoretical background is presented on polarised DIS and photon-gluon fusion. The second chapter explains the HERMES experiment. In the subsequent chapter the used Monte Carlo for this work will be described. The penultimate chapter will be devoted to analysis of the Monte Carlo data for the D^{*-}. To conclude a summary of results is presented in the last chapter.

1. Theory

1.1 Deep-Inelastic Scattering

1.1.1 Kinematics

In quantum electrodynamics (QED) the scattering of a lepton off a nucleon is, in lowest order perturbation, described as the exchange of one virtual photon. The Feynman diagram of the process is depicted in Fig. 1.1. When the photon carries a high momentum and energy, it will scatter off one of the nucleon constituents, this is *deep-inelastic scattering*. One way to characterise the scattering process, is by the four-momentum transferred from the lepton to the nucleon, $q = k - k'$. k and k' denote the initial and final lepton momentum. The four-momentum squared is a Lorentz invariant, q^2. Alternatively Q^2 is used which is [3, 4],

$$Q^2 \equiv -q^2. \tag{1.1}$$

A second invariant is the energy of the virtual photon,

$$\nu \equiv \frac{P \cdot q}{M}. \tag{1.2}$$

Here P and M are the momentum and mass of the nucleon. The final state has an invariant mass,

$$W^2 \equiv (P + q)^2 \overset{\text{lab}}{=} M^2 + 2M\nu - Q^2. \tag{1.3}$$

Observables are determined from the following kinematical relations,

$$Q^2 \equiv -q^2 \overset{\text{lab}}{=} 2EE'(1 - \cos\theta) \overset{\text{lab}}{=} 4EE' \sin^2\theta/2, \tag{1.4}$$

$$\nu \equiv q_0 \overset{\text{lab}}{=} E - E'. \tag{1.5}$$

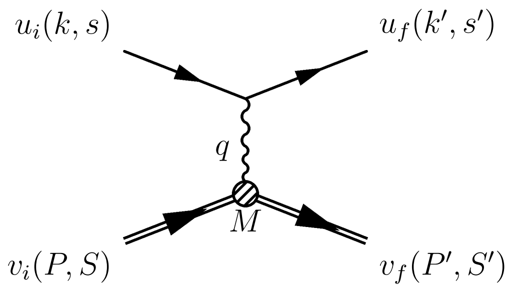

Figure 1.1: *Lepton-nucleon scattering in lowest order perturbation theory: The one-photon exchange approximation.* P, P', k, k' *are the momenta of the respective particles,* q *denotes the photon momentum.* S, S', s and s' *represent the spin of the particles and* M *denotes the mass of the nucleon.*

E and E' are the energies of the unscattered and scattered lepton respectively, with a scattering angle θ. Furthermore the dimensionless Bjorken scaling variables are defined as,

$$x \equiv \frac{-q^2}{2P \cdot q} \overset{\text{lab}}{=} \frac{Q^2}{2M\nu}, \tag{1.6}$$

$$y \equiv \frac{P \cdot q}{P \cdot k} \overset{\text{lab}}{=} \frac{\nu}{E}. \tag{1.7}$$

The first variable, x, ranging from 0 to 1, is a measure of the *inelasticity* of the process. $x = 1$ corresponds to elastic scattering. The y variable is the fraction of the initial lepton energy transferred by the photon to the nucleon.

1.1.2 Interaction

In the one-photon exchange approximation a leptonic current j^μ couples to a hadronic current J^ν via a photon propagator, $-i\frac{g_{\mu\nu}}{q^2}$. The matrix element for this process is described by [5],

$$-i\mathcal{M} = j^\mu(-i\frac{g_{\mu\nu}}{q^2})J^\nu. \tag{1.8}$$

The lepton current is described by,

$$j^\mu = \bar{u}_f(k',s')\ (ie)\ \gamma^\mu u_i(k,s), \tag{1.9}$$

where u_i and u_f stand for initial and final state spinors. This current is calculable within QED. The hadronic current is described as,

$$J^\nu = \bar{v}_f(P', S')\ (ie)\ \Gamma^\nu v_i(P, S), \tag{1.10}$$

in which Γ^ν describes the transition between the extended hadronic states v_i and v_f. This current cannot be calculated from first principles as the nucleon is not a point particle. In the HERMES kinematic range, perturbation theory does not hold for calculating the internal structure of the nucleon. However phenomenologically one can describe it by parameterising the hadron structure.

The cross-section follows from Fermi's golden rule [5],

$$\frac{d\sigma}{d\Omega} = \frac{2\pi\rho(E_f)}{\mathcal{F}} \mathcal{M}\mathcal{M}^* \bigg|_{E_f=E_i}. \tag{1.11}$$

Where $\rho(E_f)$ is the density of final states, and $\mathcal{F}$ is a flux factor or current density of incoming particles. This amounts to the general form,

$$\frac{d^2\sigma}{d\Omega dE'} = \frac{\alpha^2 E'}{q^4 E} L^{\mu\nu} W_{\mu\nu}. \tag{1.12}$$

Here α is the fine structure constant, $L^{\mu\nu}$, is the leptonic tensor, describing the photon-lepton vertex. This tensor is expressed with the current 1.9,

$$L^{\mu\nu} = j^\mu j^{\nu *}. \tag{1.13}$$

$W_{\mu\nu}$ is the hadronic tensor, describing the photon-hadron vertex, expressed with the hadron current 1.10 [6],

$$W_{\mu\nu} = J_\mu J_\nu^*\ \delta^4\left(\sum_i p_i - p'_n\right). \tag{1.14}$$

The delta function ensures conservation of energy and momentum.

One can decompose both tensors in parts symmetric and antisymmetric in μ and ν, independent and dependent on spin respectively. The hadronic tensor can be written [6] explicitly as:

$$W_{\mu\nu}(\mathrm{q};\mathrm{P},\mathrm{S}) = W_{\mu\nu}^{(S)}(\mathrm{q};\mathrm{P}) + iW_{\mu\nu}^{(A)}(\mathrm{q};\mathrm{P},\mathrm{S}). \tag{1.15}$$

Both terms of this tensor can be parameterised in a general way [6],

$$\begin{aligned}\frac{1}{2M}W_{\mu\nu}^{(S)}(\mathrm{q};\mathrm{P}) = W_1(\mathrm{P}\cdot\mathrm{q},\mathrm{q}^2)\left(-g_{\mu\nu}+\frac{q_\mu q_\nu}{q^2}\right)+ \\ W_2(\mathrm{P}\cdot\mathrm{q},\mathrm{q}^2)\frac{1}{M^2}\left[\left(P_\mu-\frac{p\cdot q}{q^2}q_\mu\right)\left(P_\nu-\frac{p\cdot q}{q^2}q_\nu\right)\right],\end{aligned} \tag{1.16}$$

$$\begin{aligned}\frac{1}{2M}W_{\mu\nu}^{(A)}(\mathrm{q};\mathrm{P},\mathrm{S}) = \epsilon_{\mu\nu\kappa\lambda}q^\kappa\Big\{G_1(\mathrm{P}\cdot\mathrm{q},\mathrm{q}^2)MS^\lambda+ \\ \frac{G_2(\mathrm{P}\cdot\mathrm{q},\mathrm{q}^2)}{2M}\left[(P\cdot q)S^\lambda-(S\cdot q)\,P^\lambda\right]\Big\}.\end{aligned} \tag{1.17}$$

Usually the functions are presented in a slightly modified form [6],

$$F_1(x,Q^2) \equiv MW_1(\nu,Q^2), \tag{1.18}$$

$$F_2(x,Q^2) \equiv \nu W_2(\nu,Q^2), \tag{1.19}$$

$$g_1(x,Q^2) \equiv M^2\nu G_1(\nu,Q^2), \tag{1.20}$$

$$g_2(x,Q^2) \equiv M\nu^2 G_2(\nu,Q^2). \tag{1.21}$$

The response of the nucleon can be described by F_1, F_2, g_1 and g_2, called *structure functions*. The polarisation independent structure functions F_1 and F_2 appear to be independent of Q^2 in a large region of this variable. Bjorken predicted this behaviour and called it *scaling*. He argued that when $\nu, Q^2 \to \infty$, and x fixed, the unpolarised structure functions only depend on the scaling variable x. An interpretation of the scaling behaviour was given by Feynman. He suggested in his *parton model* that the lepton is scattering elastically off free point-like constituents of the nucleon, the partons. In this framework the Bjorken variable x is the fraction of the momentum of the nucleon carried by the struck parton[1], see Fig. 1.2.

Measurements of the scaling behaviour of the partons have been performed with high precision. (See Fig. 1.3). At very low partonic momenta, *i.e.* at low x, scaling is violated. Also at high x scaling is only approximate, this violation is less than it is at low x. The maximum of the structure function ('probability') shifts to lower values of x when the nucleon is probed at a higher Q^2.

---

[1] This is actually only *exact* in the so-called *infinite-momentum* frame, where the nucleon is boosted to infinite momentum, hence due to time dilation the partons will not interact, and will be free particles. Scaling would be violated if this were not the case.

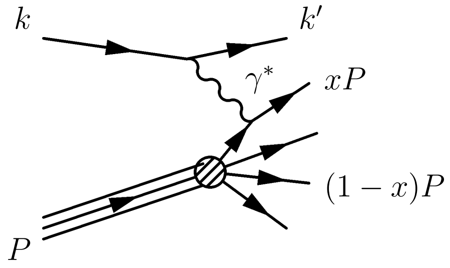

Figure 1.2: *Deep-inelastic scattering in the parton model, the struck quark has momentum xP.*

One can explain these phenomena by assuming that the quarks are interacting particles. A hypothesis for the high-x violation is gluon radiation from quarks: Quarks at high momentum lose energy by radiating gluons. The density of high-momentum quarks is reduced, and the chance of coupling to a high-momentum quark is reduced. The low-x violation can be explained by assuming that the gluons split into quark anti-quark pairs. These $q\bar{q}$ pairs are called *sea quarks*, as opposed to the *valence quarks*, probed at lower Q^2. One might say that with increasing Q^2, the resolution increases, the photon couples to softer (lower x) quarks. This is depicted in Figure 1.4.

1.1.3 Spin-Dependent Deep-Inelastic Scattering

The particles involved in the scattering have a spin degree of freedom. The coupling of the virtual photon to the target is spin-dependent. This can easily be seen as the beam and target particles are fermions with spin $\frac{1}{2}$, the spin vector projection of a fermion can have only two directions, $s_z = \pm\frac{1}{2}$. The helicity[2] of the virtual photon is $\lambda = \pm 1$. In order to obey conservation of angular momentum, only a quark with the spin direction opposite to that of the photon can absorb it. The distribution of quarks *and anti-quarks* with their spin aligned with the nucleon spin is designated q^+, the quark distribution of quarks and anti-quarks with oppositely aligned spin is denoted q^-. Distribution functions of polarised quarks with flavour f can then be defined as: $\Delta q_f(x) \equiv q_f^+(x) - q_f^-(x)$. In the naive quark parton model one can write the structure functions $F_1(x)$ and $g_1(x)$, in terms of the sum and

---

[2] Helicity is the direction of spin projected onto the direction of momentum, $\lambda = \sigma \cdot p$

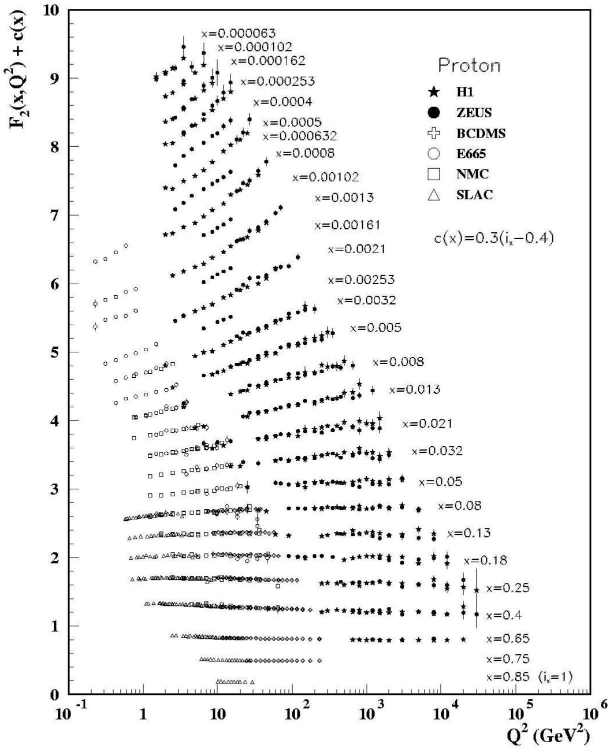

Figure 1.3: *Proton structure function F_2 plotted against Q^2 for different values of x. Scaling violations can clearly be seen at lowest x values. Figure taken from [7].*

the difference of the quark distributions q^+ and q^-:

$$F_1(x) = \frac{1}{2}\sum_f e_f^2(q_f^+(x) + q_f^-(x)) = \frac{1}{2}\sum_f e_f^2 q_f(x), \tag{1.22}$$

$$g_1(x) = \frac{1}{2}\sum_f e_f^2(q_f^+(x) - q_f^-(x)) = \frac{1}{2}\sum_f e_f^2 \Delta q_f(x). \tag{1.23}$$

Here it is assumed that the quarks are nearly massless and collinear[3]. Deviations in the structure function g_1 can be an indication of other sources

---

[3] Collinear: the spins are arranged along one line.

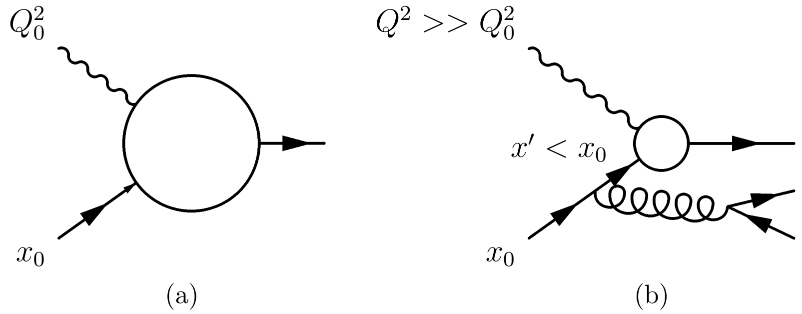

(a) (b)

Figure 1.4: *Probing at higher Q^2, the photon is more likely to strike softer quarks. The resolution of the probe has increased, this is depicted by the reduced radius of the circle.([3, 5, 4])*

of spin. In practice it is hard to obtain specific information from scaling violations of g_1, due to model dependencies and extrapolation errors [3, 8].

It is assumed that the total spin of the nucleon can be decomposed into several contributions of sources of spin,

$$S_z = \frac{1}{2}\Delta\Sigma + \Delta g + L_z. \tag{1.24}$$

In this equation $\Delta\Sigma = \sum_f \Delta q_f$ is the total[4] quark spin contribution, Δg denotes the gluonic spin contribution and L_z is the orbital angular momentum of the partons. The polarised gluon distribution is defined in a similar way as the polarised quark distribution functions: $\Delta g(x) \equiv g^+(x) - g^-(x)$.

One can relate macroscopic quantities as the nucleon spin to microscopic quantities like the polarisation of the partons via so-called sum-rules. From QCD calculations in combination with operator product expansion an integral for the total polarisation can be evaluated. This integral, known as the Ellis-Jaffe sum rule, is calculated for the proton (p) and neutron (n) to be [9]:

$$\Gamma^{p(n)} = \int_0^1 dx\ g_1^{p(n)}(x) = \frac{1}{12}\left\{\Delta C_{NS}\left((-) + a_3 + \frac{1}{\sqrt{3}}a_8\right) + \Delta C_S \frac{4}{3} a_0\right\}. \tag{1.25}$$

---

[4] Containing valence-quarks and sea-quarks.

The functions ΔC_{NS} and ΔC_S refer to the non-singlet and singlet states of the quarks, calculable from QCD. In the quark parton model the a_j are related to the quark distributions $\Delta q_f = \int_0^1 dx \Delta q_f(x)$ as:

$$\begin{aligned} a_0 &= \Delta\Sigma = \Delta u + \Delta\bar{u} + \Delta d + \Delta\bar{d} + \Delta s + \Delta\bar{s}, && (1.26) \\ a_3 &= \Delta q_3 = \Delta u + \Delta\bar{u} - (\Delta d + \Delta\bar{d}), && (1.27) \\ a_8 &= \Delta q_8 = \Delta u + \Delta\bar{u} + \Delta d + \Delta\bar{d} - 2(\Delta s + \Delta\bar{s}). && (1.28) \end{aligned}$$

a_3 and a_8 are calculated via hyperon decay rates and beta decay. a_0 cannot be calculated in this way, but may be extracted by measuring $\Gamma^{p(n)}$. By assuming that Δs and $\Delta\bar{s}$ are zero, one can then also solve the equations for the separate quark flavours.

When taking QCD in to account, a correction due to the gluons arises. As this is *anomalous* with respect to the quark parton model interpretation it is called the *axial anomaly* [9],

$$a_0 = \Delta\Sigma - n_f \frac{\alpha_s(Q^2)}{2\pi} \Delta g(Q^2). \tag{1.29}$$

One can see that determination of a_0 does not yield a direct value for $\Delta\Sigma$, but rather it contains the gluonic contribution as well. The EMC experiment at CERN found that a_0 is low. At the time this result was interpreted within the quark parton model, in which it was assumed that $a_0 = \Delta\Sigma$. But as seen in QCD, the small value may be due to the fact that the gluons contribute a sizable amount. In which case the measured value a_0 would be low but not $\Delta\Sigma$ and Δg. It is therefore important to search for different approaches to either $\Delta\Sigma$ or Δg. An investigation into $\Delta\Sigma$ was done previously by a semi-inclusive flavour decomposition of the nucleons [4].

Since leptons do not couple directly to gluons, it is not possible to measure Δg directly. A mechanism to obtain information about the gluon polarisation is *photon-gluon fusion*. Experimental signatures for photon-gluon fusion include high transverse momentum final states and heavy quark production. The high transverse momentum channels are overwhelmed by background from QCD-Compton radiation. This effect is negligible when looking at heavy quarks.

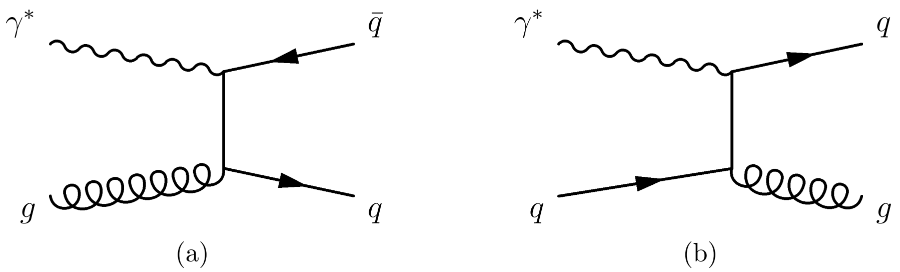

Figure 1.5: *(a) Photon-gluon fusion and (b) QCD Compton to* $\mathcal{O}(\alpha \cdot \alpha_s)$.

1.2 Heavy Quark Production Near Threshold

1.2.1 Photon-Gluon Fusion

The main process contributing to heavy quark production in lepton-nucleon scattering at HERMES is photon-gluon fusion (Fig. 1.5a). A virtual quark anti-quark pair, produced by a fluctuating gluon, is put on mass-shell by absorbing the virtual photon. At HERMES charmed mesons and baryons are produced at low values of Q^2. The formal limit for so-called *photo-production* is $Q^2 \to 0$. The reason for studying photo-production of charmed mesons is the relative cross-section of charmed mesons is largest in the photo-production region [10].

The center-of-momentum energy of the photon-gluon system can be written as,

$$\hat{s} = (p_g + q)^2 = (P_Q + P_{\bar{Q}})^2, \tag{1.30}$$

where p_g is the gluon momentum, q is the photon momentum, $P_{Q/\bar{Q}}$ are the momenta of the produced quark and anti-quark respectively.

The gluon momentum fraction of the total nucleon momentum is,

$$x_g = \frac{p_g \cdot q}{P \cdot q} = x_{Bj} \left(1 + \frac{\hat{s}}{Q^2}\right), \tag{1.31}$$

where x_{Bj} is the Bjorken x variable as defined in Eq. 1.6.

Due to the large mass of the charm quark it is possible to give a perturbative description of photo-production of charm in QCD [10, 11]. The unpolarised and polarised partonic photon-gluon fusion cross-sections for photo-production have been calculated to leading order [8, 12, 13] to be,

$$\hat{\sigma}_{\gamma g}(\hat{s}) = \frac{2\pi\alpha\alpha_s(Q^2)}{\hat{s}}\left[-\beta(2-\beta^2)+\frac{1}{2}(3-\beta^4)\ln\frac{1+\beta}{1-\beta}\right], \tag{1.32}$$

$$\Delta\hat{\sigma}_{\gamma g}(\hat{s}) = \frac{2\pi\alpha\alpha_s(Q^2)}{\hat{s}}\left[3\beta-\ln\frac{1+\beta}{1-\beta}\right]. \tag{1.33}$$

The parameter $\beta = \sqrt{1-4m_Q^2/\hat{s}}$ is the center-of-mass velocity of the produced quarks.

In Fig. 1.6 the partonic photon-gluon fusion cross-section is plotted as a function of the center-of-mass energy in this system. The cross-section has a sharp rise at the heavy quark production threshold, and then decreases asymptotically. The cross-section for photo-production of a heavy quark anti-quark pair on a nucleon can be written as a convolution of the gluon density and the partonic cross-section (Eqs. 1.32, 1.33) [8, 12, 13],

$$\sigma_{\gamma N\to q\bar{q}X} = \int \mathrm{d}\hat{s}\;\hat{\sigma}_{\gamma g}(\hat{s})\;g(x_g,\hat{s}), \tag{1.34}$$

$$\Delta\sigma_{\gamma N\to q\bar{q}X} = \int \mathrm{d}\hat{s}\;\Delta\hat{\sigma}_{\gamma g}(\hat{s})\;\Delta g(x_g,\hat{s}). \tag{1.35}$$

1.2.2 Asymmetry

The photo-production cross-section (Eqs. 1.34, 1.35) depends on the (polarised) gluon density. Hence by measuring heavy quark production cross-sections of polarised electrons on a polarised nucleon one can extract information on the gluon polarisation. However in practice a cross-section *asymmetry* is determined. The asymmetry for *longitudinally* polarised nucleon target and lepton beam is defined as:

$$A_{\parallel} \equiv \frac{\sigma^{\overset{\Leftarrow}{\rightarrow}} - \sigma^{\overset{\Rightarrow}{\rightarrow}}}{\sigma^{\overset{\Leftarrow}{\rightarrow}} + \sigma^{\overset{\Rightarrow}{\rightarrow}}}. \tag{1.36}$$

Here $\Rightarrow, \Leftarrow$ denotes the polarisation direction of the target and $\rightarrow$ designates beam polarisation.

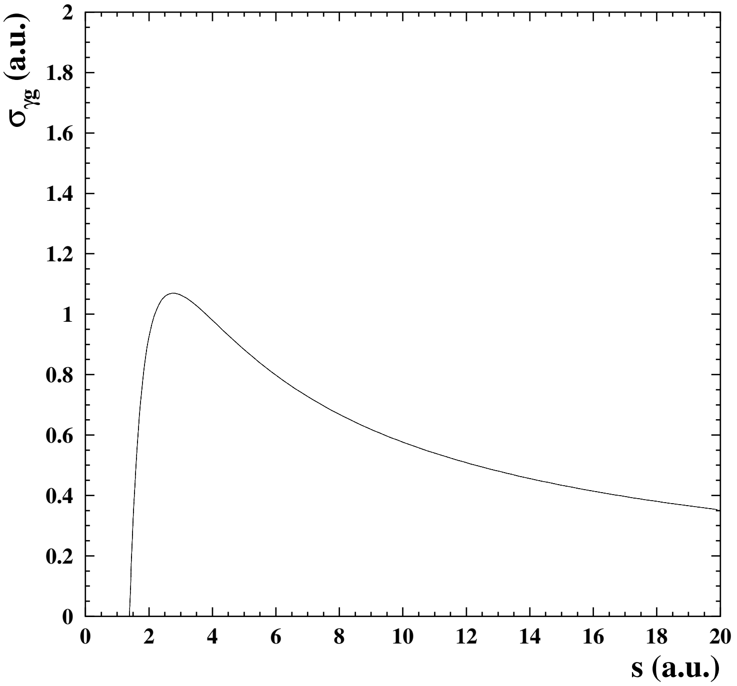

Figure 1.6: *The photon-gluon fusion cross-section at partonic level as function of the center-of-mass energy in the $q\bar{q}$ system. Calculated from (1.32).*

The photon-nucleon asymmetry is defined as,

$$A_{\gamma N}^{q\bar{q}} \equiv \frac{\Delta\sigma_{\gamma N\rightarrow q\bar{q}X}}{\sigma_{\gamma N\rightarrow q\bar{q}X}} = \frac{\int \mathrm{d}\hat{s}\ \Delta\hat{\sigma}_{\gamma g}(\hat{s})\ \Delta g(x_g,\hat{s})}{\int \mathrm{d}\hat{s}\ \hat{\sigma}_{\gamma g}(\hat{s})\ g(x_g,\hat{s})}. \tag{1.37}$$

The partonic cross-section and the gluon distribution can be deconvolved assuming that in a small interval of the invariant mass[5], $\hat{s}$, the gluon distributions, g and Δg are nearly constant [14]. One can then write,

$$A_{\gamma N}^{q\bar{q}} \approx \frac{\Delta\hat{\sigma}_{\gamma g}}{\hat{\sigma}_{\gamma g}}\frac{\Delta g}{g} = \hat{a}_{PGF}\ \frac{\Delta g}{g}. \tag{1.38}$$

---

[5] As is the case in HERMES.

$\hat{a}_{PGF}$ is called the asymmetry for photon-gluon fusion at partonic level, and is specific for the partonic process.

In practice an asymmetry of *lepton-nucleon* scattering is determined. The relation of the lepton-nucleon asymmetry to the photon-nucleon asymmetry is given by,

$$A_{lN}^{q\bar{q}} = D\, A_{\gamma N}^{q\bar{q}}, \qquad (1.39)$$

here D is the photon *depolarisation factor*, which tells how much of the polarisation is transferred from the lepton to the photon.

1.3 Fragmentation

As soon as the quarks are produced in the photon-gluon fusion they form hadrons because of colour-confinement. The process in which the hadron formation takes place is called *hadronisation* or quark *fragmentation*. Fragmentation is poorly understood, especially near a production threshold [12]. The charm quarks in HERMES are produced near threshold, this poses some problems in correct modelling as at low Q^2 no perturbative QCD calculation can be made.

The hadrons formed by the fragmenting charm quarks can also contain quarks of the target nucleon. The produced charmed hadrons will include D-mesons and baryons, *e.g.* the Λ_c^+. The LUND string model is one of a few models which are implemented in the used Monte-Carlo to describe the fragmentation process. It will be described briefly in chapter 3.

The kinematical phase space which is used, depends on the mass of the produced quarks, and it's visibility is limited by the detector. The center-of-mass energy in HERMES is not much higher than the mass of two charm quarks. This means that the average momentum of the quarks in the rest frame is small. The quarks are produced back-to-back in the photon-gluon center-of-momentum frame. Therefore, due to the boost in the HERMES kinematics, the charmed mesons will be emitted at low forward angles with respect to the beam.

The basis of the analysis presented in this thesis is the D^{*-} meson originating from photon-gluon fusion events. HERMES has a center-of-mass energy of 7 GeV. A D^* meson has a mass of 2.010 GeV [7]. Considering that charmed particles are produced in pairs, in which each particle carries one charm quark, the threshold energy for creating charmed mesons is thus around 4 GeV. At HERMES kinematics this means that the total momentum of the charmed particles can be at most 3 GeV in the center-of-mass frame.

1.4 Decay Modes

1.4.1 Hadronic Decays

The D^* mesons decay via the strong or electromagnetic interaction into the D mesons. These mesons decay into a multitude of hadronic final states listed in Table 1.1. Unfortunately analysis of these modes is hindered by a large background (*cf.* [15]).

1.4.2 Semi-Leptonic Decays

The semi-leptonic decay of D^{*-} has an advantage over the other ones, and is thus taken as a basis for analysis. In Table 1.2 the semi-leptonic modes with highest branching ratios are stated.

The neutrino indicates that this decay should go via the *weak* interaction. The diagrams of the decay channel investigated in this thesis are drawn in Fig. 1.7. In the weak decay an electron is formed, which can be easily detected in the background of scattered HERA beam positrons. Together with

	Decay Channel	Branching Fraction (%)
D^{*+}	$\rightarrow D^0\pi^+$	67.7 ± 0.5
	$\rightarrow D^+\pi^0$	30.7 ± 0.5
	$\rightarrow D^+\gamma$	1.6 ± 0.4
D^0	$\rightarrow K^-\pi^+$	3.80 ± 0.09
	$\rightarrow \overline{K^0}\pi^0$	2.28 ± 0.22
	$\rightarrow \overline{K^0}\pi^+\pi^-$	5.92 ± 0.35
	$\rightarrow K^-\pi^+\pi^0$	13.1 ± 0.9
	$\rightarrow K^-\pi^+\pi^+\pi^-$	7.46 ± 0.31

Table 1.1: *Common hadronic decay modes of the D mesons [7]. The charge conjugated modes are also possible.*

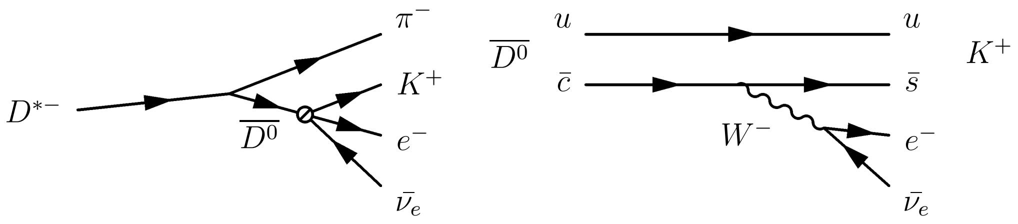

(a) (b)

Figure 1.7: *(a) Semi-leptonic decay of D^{*-}. (b) Secondary decay vertex of first diagram, weak decay of $\overline{D^0}$.*

a relatively high branching ratio, this enables a clean identification. Unfortunately the neutrino makes the reconstruction of events only *partial*. A reconstruction of the invariant mass of the produced mesons will be broadened due to a missing momentum the neutrino carries away. This also leads to a shifted invariant mass spectrum. Previous studies in the semi-leptonic channels have not been straightforward [16, 17]. This is not surprising as the PGF yield is low compared to background in photo-production.

	Decay Channel	Branching Fraction (%)
D^0	$\rightarrow K^- e^+ \nu_e$	3.58 ± 0.15
	$\rightarrow K^- \mu^+ \nu_\mu$	3.19 ± 0.18
	$\rightarrow \overline{K^0} \pi^- e^+ \mu_e$	1.8 ± 0.8
	$\rightarrow \pi^- e^+ \nu_e$	3.6 ± 0.6

Table 1.2: *Semi-leptonic decay modes of the D^0 meson with highest branching fractions [7]. Charge conjugated modes are implied.*

1.5 Background Processes

The background for quasi-real photo-production is roughly two orders of magnitude larger than the photon-gluon fusion yield [14]. To ensure that this background is suppressed, good selection criteria must be imposed. There is a fraction of events that consists of the same final state particles as produced in the D^{*-} decay. This main background for heavy quark production is production of kaons and pions in DIS. A different source consists of particles produced in the QCD-Compton process which is depicted in Fig. 1.5(b). The gluon produces a pair of lightly flavoured hadrons with a high transverse momentum. In heavy quark production the contribution by these final states to the background is negligible. Distinguishing same final states from charmed hadrons which are not a D^{*-} meson is necessary to know which contribution the D^{*-} has.

The kinematical distribution of non-charmed processes is different from the photon-gluon fusion events. This also holds for *charm background*. Decays from charmed particles not originating from a D^{*-}. These differences in kinematics are used to deselect a large fraction of the background. To know which differences can be exploited, Monte Carlo simulations are necessary to explore several kinematic distributions. A few specific restrictions have shown to offer promising results [18].

2. HERMES Experiment

2.1 Introduction

The HERMES[1] experiment is one of four located at the HERA[2] ring of the accelerator center DESY[3] in Hamburg, Germany. Commissioned in 1995, HERMES was built to investigate the spin structure of the nucleon [19]. Previous experiments at SLAC and CERN on the spin structure of the nucleon yielded surprising results. Only 20 % of the spin could be accounted for by the quarks.

To probe the nucleons, polarised positrons with a momentum of 27.5 GeV are scattered off a nuclear target. This target consists of polarised nuclei contained in a gas-cell. The target nuclei range from hydrogen or deuterium to unpolarised heavier nuclei as nitrogen and krypton. With the unpolarised targets HERMES is capable of measuring nuclear interactions, such as formation times of hadrons inside nuclear matter in deep-inelastic scattering. The particles from the DIS enter the HERMES spectrometer, which consists of various detectors for tracking and particle identification. During experiments with polarised targets, the target polarisation and gas consistency are monitored through a system which includes a polarimeter and a target gas analyser.

HERA also provides a 920 GeV proton beam, used by the three other experiments on the HERA ring. H1 and ZEUS are collider experiments that employ the proton and positron beams, and HERA-B is a fixed target experiment that only makes use of the proton beam.

---

[1] *HERA Measurement of Spin*

[2] *Hadron Elektron Ring Anlage.*

[3] *Deutsches Elektronen Synchrotron*

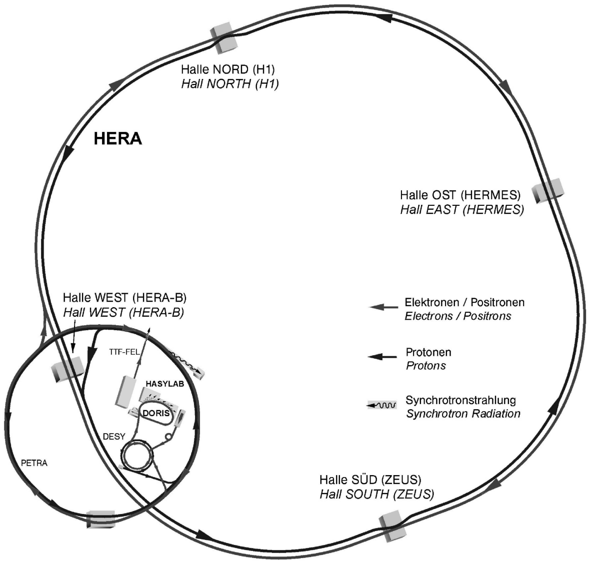

Figure 2.1: *Schematic overview of* HERA *with all experiments on the main accelerator and storage ring and the pre-accelerators. The positrons travel through the outer ring.*

2.2 Accelerators and Storage Ring

Before the positrons and protons enter the main accelerator HERA, they are pre-accelerated. The particles pass though several stages depicted in Figure 2.1: The positrons are created and are accelerated in LINAC II to gain 500 MeV. The particles are injected in PIA (positron intensity accumulator), and a beam of 60 mA is transported to DESY II, where they are accelerated to 7 GeV. The particles are injected into the storage ring in *bunches*, with a well defined spacing (and thus timing). Subsequently the positrons are fed in PETRA II[4] until 70 bunches are injected. PETRA II boosts the momentum to 14 GeV, and injects into HERA, until 210 bunches are filled. HERA, then ramps the momentum to 27.5 GeV.

---

[4] *Positron Elektron Tandem Ring Anlage*, second upgrade. In the first machine the gluon was discovered in 1979.

2.2.1 Self Polarisation: Sokolov-Ternov Effect

Due to the *Sokolov-Ternov effect* the particles in the ring become transversely polarised. Charged spin-$\frac{1}{2}$ particles have two polarisation states which are separated in energy in a magnetic field. There is an asymmetry in transition probability for parallel and anti-parallel spin states. It takes a while for all particles to align spins. Typically the self-polarisation build-up in time can be described by the following equation, if there are no depolarising effects present:

$$P = A(1 - e^{-\frac{t}{\tau}}), \tag{2.1}$$

$$\text{with } \frac{1}{\tau} = \frac{5\sqrt{3}}{8}\frac{c\lambda_c r_e}{2\pi}\frac{\gamma^5}{\rho^3}.$$

A is the equilibrium polarisation value, λ_c is the Compton wavelength, r_e the classical electron radius, ρ the magnetic bending radius, and γ is the usual relativistic Lorentz factor. The value τ describes the *typical* polarisation time.

The typical beam polarisation is around 50%. The rise time for this polarisation is about 22 minutes. HERMES utilises *spin rotators* to rotate the spin from transversely polarised to longitudinally polarised. Spin rotators are placed on either side of the experiment, so that polarisation can build up[5].

2.3 Target

In the experiment an internal gas target is used. The gas is polarised in an atomic beam source (ABS). The polarised gas is fed into a thin walled open ended elliptical tube, the target cell[20]. The target cell is contained in a magnetic holding field for keeping the nuclear polarisation. The holding field is produced by a superconducting magnet around the target cell. Optionally one can switch-off the polarised gas injection and start an unpolarised gas flow for 'nuclear effect' measurements.

The ABS injects a low density polarised gas ($10^{14} - 10^{15}$ cm^{-2}) into the target cell. In the ABS the gas molecules are dissociated using a RF

---

[5] Due to the Sokolov-Ternov effect only *transverse* polarisation is built up.

discharge. The atomic flow is passed through a cold nozzle (100 K), is collimated and sent through a Stern-Gerlach sextupole magnet to separate magnetic hyperfine states. With an RF-field the hyperfine states are populated and depopulated adiabatically to gain a high density of a specific polarisation state. Electronic polarisation is transferred to nuclear polarisation via hyperfine interactions. Next the states will be separated again, and after this a last field transition is made to have an optimal polarisation of the target nuclei.

2.4 Spectrometer

The final state particles from the reaction are measured using the HERMES spectrometer. Pictured in figure 2.2 is the HERMES spectrometer which has a forward angle because of the boost of the colliding system in the laboratory frame. The angular acceptance of the detector ranges from 40 to 220 mrad. The detectors in the spectrometer can be divided in two kinds, tracking and the particle identification. Both will be discussed in the next section.

2.4.1 Tracking

The momenta of charged particles are extracted from their deflection in the magnetic field of the spectrometer magnet, using information from the tracking detectors. The main detectors used for tracking are briefly described.

Lambda Wheels

The newest elements of the spectrometer are the Lambda wheels. These silicon strip detectors are located very close to the interaction region, and the angular acceptance is increased especially for the decay products of lambda particles.

Drift Chambers

The drift chambers contain parallel wire-sets in a space filled with a gas mixture. Particle tracks are determined from measuring the distance of the track to a wire. The electro-magnetic field of a passing particle creates slow moving electrons which will drift to the anode, read-out by a DAC. This type

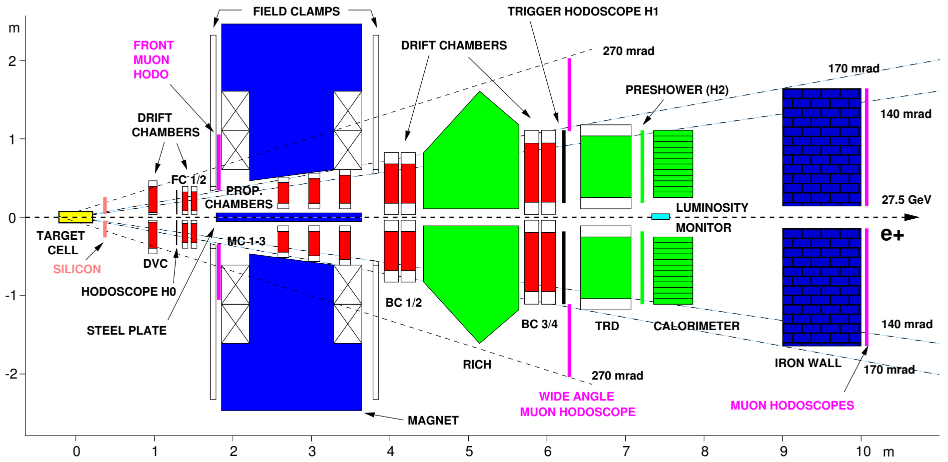

Figure 2.2: *A side-view of the HERMES spectrometer with all its components after upgrades in 2001.*

of chamber is used in front of the magnet and behind, referred to as drift vertex chamber (DVC), front chambers (FC's) and back chambers (BC's).

Proportional Chambers

Inside the magnet region proportional chambers are used for so-called *short tracks*. Particles which do not make it through the magnet can thus still provide us with momentum information.

2.4.2 Particle Identification

Particle identification is achieved using a combination of three detectors.

Ring Imaging Čerenkov Hodoscope

Especially electrons (positrons) and hadrons need to be separated in HERMES, in order to distinguish beam particles from scattered particles. A clear separation can be made with a Ring Imaging Čerenkov Hodoscope or RICH. Furthermore a number of hadron types can be clearly identified as well within a certain momentum range. The principle upon which a RICH works is Čerenkov radiation emitted from charged particles. When a charged particle moves in a medium with index of refraction n, with a greater speed (v_p) than the speed of light in that medium (c_m), it radiates energy under a specific angle according to

$$\cos\theta_c = \frac{c_m}{v_p} = \frac{1}{\beta n}. \tag{2.2}$$

In order to separate different kinds of particles, note that the *threshold* momentum[6] differs only in the mass of the particles, specifically,

$$p_t = \beta_t \gamma_t m c, \tag{2.3}$$

where $\beta_t = 1/n$ and $\gamma_t = \sqrt{1-\beta_t^2}$. Even if particles have the same momentum, the threshold momentum will differ according to their mass. This principle is used in the RICH to clearly separate protons, kaons and pions roughly in a momentum-range from 3 GeV and above [19, 4].

Transition Radiation Detector

Hadron/beam-lepton separation is achieved in the transition radiation detector or TRD. Charged particles radiate energy when traversing a boundary between two dielectrics. The energy of the radiated photons is proportional to the relativistic Lorentz factor γ. The scattered beam positrons at HERMES have $\gamma > 6000$, while hadrons will usually have $\gamma < 200$. This enables the discrimination of beam particles and scattered particles [3, 19, 4].

Preshower Trigger and Calorimeter

The calorimeter consists of photomultiplier tubes, shielded by lead glass blocks to prevent radiation damage. The calorimeter is preceded by a preshower detector. The preshower is yet another means of hadron lepton separation. As charged particles traverse the preshower trigger they release electromagnetic radiation into the calorimeter. Particle identification is based on the difference of deposited energy by leptons and hadrons in the calorimeter. [3, 19, 4].

---

[6] The momentum at which the particle just starts to radiate.

3. Monte Carlo Simulation

3.1 Introduction

In this chapter the Monte Carlo simulations for the production of D^{*-} mesons and other processes are presented. First the software used to generate the the various processes will be introduced. Next, the digitisation and tracking of the simulated events in the HERMES spectrometer will be discussed.

3.2 Simulation Software

3.2.1 Event Generators

The used heavy flavour Monte Carlo, AROMA, is built on LEPTO [21], a general DIS generator. The letter generator contains the kinematics of the (unpolarised) DIS and several parameterisations of parton densities that describe the data. The scattering cross-sections are calculated using next-to-leading order (NLO) QCD processes. Hadronisation of the partons is calculated through *fragmentation functions*. Fragmentation functions are not calculable from perturbative QCD, as they involve long distance, and thus low Q^2 processes [4]. In LEPTO the LUND string fragmentation model [22] is used. This model includes quark production from the colour field. The gluon potential is modelled as a linear function. When the potential energy reaches twice the quark mass, new quarks can be created.

AROMA 2.2 [23, 24] is a *slave* program of LEPTO and includes DIS as well as photo-production kinematics. It uses the hadronisation model and multiple variables like quark masses and parton densities from LEPTO. Gluon bremsstrahlung and *jets* are modelled through *parton shower* algorithms. Parton showers are produced by accelerated coloured objects, comparable to electrodynamics. The gluon participating in the fusion process has been given a small initial transverse momentum, implemented with a Gaussian distribution. This can be understood as *Fermi motion* of the partons in the nucleon [22]. Phase space points are calculated making use of a cross-section formula similar to Eq. 1.34, consecutively they are quasi-randomly sampled. Not included in AROMA are intrinsic charm and resolved photon processes, as these play an insignificant role at HERMES kinematics.

Other processes in which the same particles are produced as in the decay of a D^{*-} (π^-, K^+ e^-) are simulated with the DIS generator PYTHIA 6.2 [25, 26]. PYTHIA allows for a much broader spectrum of production mechanisms than AROMA. A full range of physics processes can be found in [26]. For the analysis presented in this work, previously generated PYTHIA Monte Carlo data were analysed [17].

3.2.2 Event Selection

To parse only events that correspond to decay products with an invariant mass close to the D^{*-} meson, the events have been selected before they are written to the output file. The Monte Carlo generator (GMC) allows for settings which describe what events will be parsed or rejected. The option `/GMC/SET UseSelector 1` will tell the generator to look in a so-called selector file to apply initial cuts which are optimised for the generation of a particular set of particles. For the generation of the D^{*-} meson, the used settings were:

- require particles in HERMES acceptance,
- particles use kinematical values from GMC,
- require "$\overline{D^0}$" (K^+ and e^-) to have invariant mass between 0.6 and 2.1 GeV,
- require "D^{*-}" ("$\overline{D^0}$" + π^-) to have invariant mass between 0.6 and 2.5 GeV.

To obtain mostly events from a D^{*-} decay, the PID was assumed to be *perfect*, *i.e.* a particle in the generator can be identified without error.

For the generation of 'background events', however, the events were generated with the following settings [17]:

- require particles in HERMES acceptance,

- particles use kinematical values from GMC,
- π is any of μ, π, K or p in acceptance with momentum between 0.2 and 2.2 GeV,
- electron is any e^+ or e^- in acceptance,
- mass difference of "K, e, π" and "K, e" is less than 500 MeV.

It is called a *semi-perfect* PID, to allow for mismatch of particles in the simulated detectors.

3.2.3 Digitisation

The event files produced by the generator are fed into the digitiser program (HMC). HMC calculates any interaction of the particles within the detector. A model of the detector is programmed in GEANT. The detector is programmed as a series of *sensitive volumes*. These in turn are divided into *detector volumes* and *secondary volumes*. The detector volume participates in the simulated *detection*, while the secondary volume is needed in the simulation of material interactions like multiple scattering. The interactions with the detector volumes are calculated by means of *digitisation* of the volume. The particle will interact with the detector, *e.g.* with a wire chamber, which will in turn produce a simulated pulse. The interaction with the detector is called a *hit*. All the hits are *digitised*, and saved in ADAMO tables.

Furthermore the motion of the particles is influenced by the detectors, this is also calculated within HMC. As the particle interacts with a volume its track is determined to the next hit position. Secondary particles, like delta electrons, are also modelled in HMC. Their interactions are digitised as well.

Radiative corrections are calculated as well. GEANT enables a simulation of events which is very close to data. In order to digitise the MC events, correct geometry and GEANT information is supplied to HMC, before the GMC event file is processed [27].

3.2.4 Track Reconstruction

To reconstruct the *tracks* of the simulated particles, the interaction points in the various detectors must be combined to directions in space. The main steps to go through in order to obtain this information are as follows.

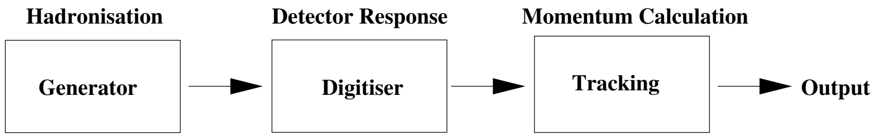

Figure 3.1: *The used Monte Carlo Chain.*

- Tree search algorithm
- Track combination
- Momentum lookup

The Hermes Reconstruction Code (HRC) was used for this purpose. In the *tree search* routine the most likely track is reconstructed from the interaction points. The momentum of the particles is deduced from the bending angle in the modelled magnetic field [27].

3.3 MC Production

The described software has been installed in the local computing environment. HERMES Monte Carlo release number 19 was used for the production of the signal events. The generator (GMC), digitisation and detector simulation (HMC) and tracking (HRC) parts of the Monte Carlo have been connected by a dedicated script developed for this purpose. A diagram of the software chain is depicted in Fig. 3.1. The output files of each subsequent part, in ADAMO format, were saved to disk before being processed by the next link. Thus multiple MC *runs* could be initiated on multiple computers, enabling a greater production speed.

With the Monte Carlo program AROMA, 2 10^4 events were produced which were tracked through HMC and HRC. For the non-charmed background, 5 10^6 events, produced by PYTHIA, were taken for the analysis.

ADAMO enables all information to be stored on an event-by-event basis. For each event the relevant information like produced particle types, momenta and energies is stored. For the analysis of the MC events stored in the ADAMO tables, these files were translated to *ntuple* files. For the translation a program was written in the HANNA frame. HANNA is a C framework that synchronises the information in the ADAMO tables per event. The ntuples are subsequently analysed in the FORTRAN77 environment *Physics Analysis Workstation.*

4. Analysis

4.1 Introduction

In this chapter the analysis of the π^-, e^-, K^+ particles originating from the semi-leptonic decay of the D^{*-} is discussed and the results are presented. The analysis is performed for two types of events: Events from $D^{*-} \rightarrow \overline{D^0} + \pi^- \rightarrow e^- K^+ \pi^-$, and events in which the π^- is not emitted in the D^{*-} decay. The first category is most interesting because the momenta of the particles involved are more characteristic for the decay process. If the pion doesn't originate from the D^{*-} decay but from the decay of the D meson, the first step is either $D^{*-} \rightarrow D^- + \gamma$ or $D^{*-} \rightarrow D^- + \pi^0$. Hence, in addition to the π^-, K^+, e^- particles a γ or π^0 is emitted.

The analysis is organised as follows. First the data is selected. Next momentum distributions are investigated and a search is done for correlation between these momenta. Thirdly, a reconstruction of the invariant mass of the e^-, K^+ system is performed. An investigation of correlations between the reconstructed e^-, K^+ mass and the pion momenta is performed. Lastly a reconstruction of the $\pi^- K^+ e^-$ mass is made and the mass-difference distribution $\Delta M = M_{\pi^- K^+ e^-} - M_{K^+ e^-}$ is investigated.

First, the results of the calculations performed with AROMA are discussed in detail, this is followed by a global discussion of the MC data obtained with PYTHIA.

4.2 Data Selection

The first step in the analysis of the MC events is the data selection. Events from the semi-leptonic decay of the D^{*-} meson contain one pion, one kaon and one electron. Therefore, the same restriction is made for the MC data, thus reducing the combinatoric background. Next the ranges of the pion and electron momenta are reduced. Due to the small mass-difference between the D^{*-} and $\overline{D^0}$ mesons, the pion momentum is smaller than 2 GeV.

4.3 Analysis Strategies

From the kinematical variables determining this decay, a few have been subjected for a further investigation. First of all a comparison is made of the momentum distributions of the K, e and π originating from a $D^{*-} \to \overline{D^0}\pi^- \to K^+e^-\pi^-$ decay and other modes with the same particles in the final state. The kaon and electron from the $D^{*-} \to \overline{D^0}$ decay will mostly have a combined momentum of greater than 4.5 GeV. Since the pion originates in the $D^{*-} \to \overline{D^0}$ decay, a correlation is expected between the pion momentum and the invariant mass of the $\overline{D^0}$. Another important analysis method is the mass *difference* between the reconstructed D^{*-} and the $\overline{D^0}$. When all particles from D^{*-} ($\overline{D^0}$) decay could be detected, the masses of those particles can be completely reconstructed, and the $\Delta M = M(D^{*-}) - M(\overline{D^0})$ can be calculated. The determination of $\Delta M = M(\pi,\ K,\ e) - M(K,\ e)$ is also a valuable tool if the D^{*-} and the $\overline{D^0}$ masses are only partially reconstructed. Next, the angular dependencies of the decay products have been investigated. Because of the small mass-difference of the D^{*-} and the $\overline{D^0}$, the pion and $\overline{D^0}$ acquire almost no momentum in the D^{*-} restframe. This means the $\overline{D^0}$ and the π^- are emitted approximately in the direction of the D^{*-}, with the consequence that the momenta of e^-, K^+ and the pion are correlated. This correlation is reflected by the emission angles of the e^- and K^+ with respect to the pion momentum.

4.4 Analysis of the data obtained from AROMA

The momentum distributions of the particles emitted in the decay $D^{*-} \to \overline{D^0}\pi^- \to K^+e^-\pi^-$ are shown in Fig. 4.1a. As is visible from the figure, Monte Carlo simulations demonstrate that almost all pions from D^{*-} decay have a momentum smaller than 2 GeV. Fig. 4.1b shows the momentum distributions of particles in events in which the pion originates from other charmed hadrons.

As will be shown later, in PYTHIA calculations (Fig. 4.7) it is observed

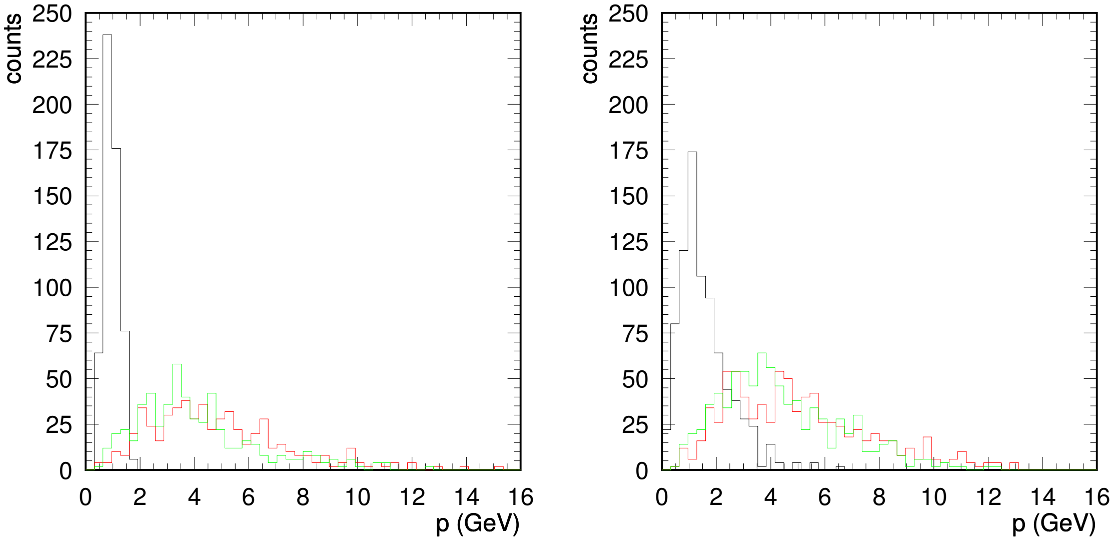

(a) (b)

Figure 4.1: *Distribution of pion, electron and kaon momenta. Pion originating from (a) $D^{*-} \rightarrow \overline{D^0}\,\pi^-$ decay and (b) other decay modes (AROMA).*

that the electrons not originating in decay of charmed particles, have a high abundance below momenta of 1.5 GeV. On the contrary, electrons originating in a decay of charmed particles are scarce below a momentum of 1.5 GeV (Fig. 4.1). Hence, a restriction on electron momentum was set in order to select mostly electrons from D^{*-} decay. Pion and electron momentum restrictions are,

$$p_\pi < 2\ \text{GeV},\ p_e > 1.5\ \text{GeV}. \tag{4.1}$$

The momenta of the kaon and electron from the $\overline{D^0}$ are correlated. Fig. 4.2 shows that the summed momenta of the kaon and electron are most likely higher than 4.5 GeV. This holds for the events in which the pion originates from a D^{*-} decay, as well as for events in which the pion was emitted in other decay modes. However in events with particles from non-charmed hadrons, the abundance of slow electrons and kaons is much higher, (*cf.* Fig. 4.8b). Considering this, a restriction can be placed on the combined kaon and elec-

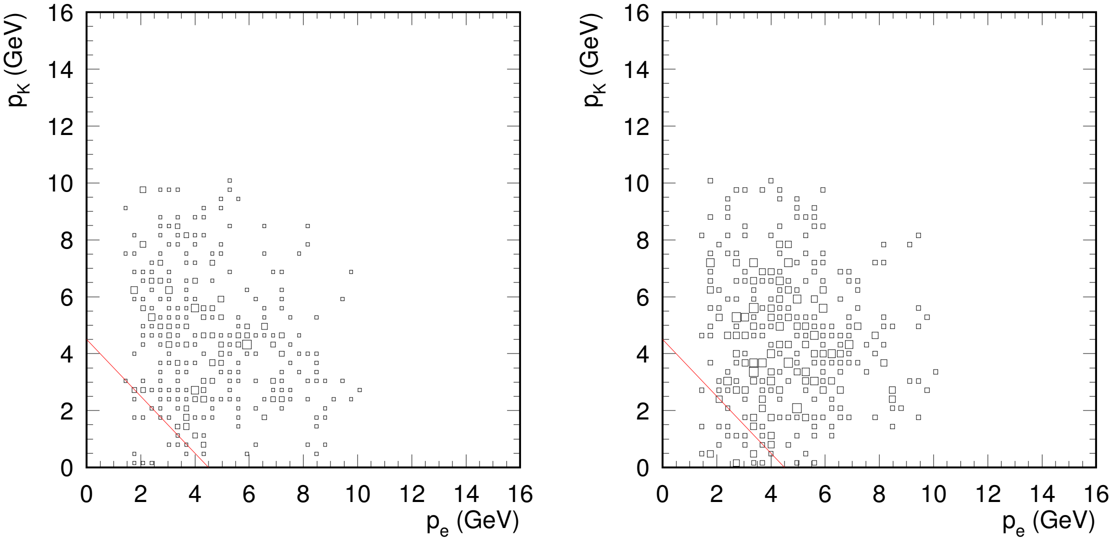

(a) (b)

Figure 4.2: *Momenta of electron versus kaon calculated from AROMA. Pion originating in (a)* $D^{*-} \rightarrow \overline{D^0}\pi^-$ *decay and (b)* π^- *from other decay modes. Restrictions 4.1 are applied.*

tron momentum to obtain mostly particles from D^{*-} decay:

$$(p_K + p_e) > 4.5 \text{ GeV}. \tag{4.2}$$

Since the pion acquires a relatively small momentum in the rest frame of the decaying D^{*-}, the angles between the pion and the $\overline{D^0}$ will be small. A comparison of the angles between the decay products of the $\overline{D^0}$ and the pion shows a strong correlation if the pions are emitted in a D^{*-} decay (Fig. 4.3a). This correlation cannot be seen in events in which the pion originated from the decay of other particles. The restriction on the angles between the decay products is,

$$\begin{aligned} (1-\cos\theta_{\pi e}) &< 0.02 \\ (1-\cos\theta_{\pi K}) &< 0.02 \\ (1-\cos\theta_{\pi e})(1-\cos\theta_{\pi K}) &< \frac{(0.014)^2}{2}. \end{aligned} \tag{4.3}$$

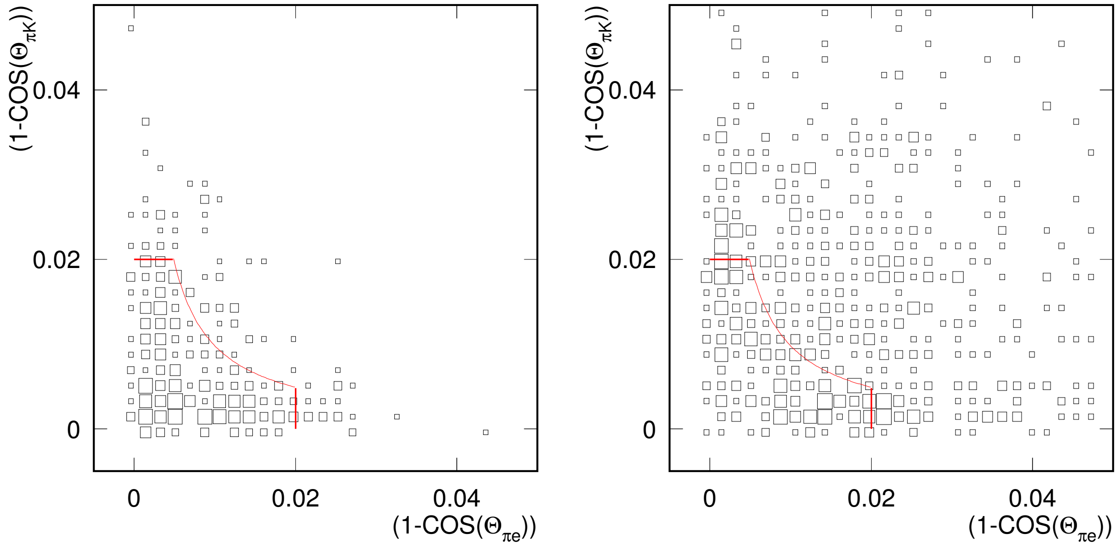

(a) (b)

Figure 4.3: *Opening angles between the momenta of the e and π versus angles between momenta of e and K. Pion originating from (a) $D^{*-} \rightarrow \overline{D^0}\ \pi^-$ decay and (b) other decay modes (*AROMA*). Restrictions 4.1, 4.2 are applied.*

Figs. 4.3a and 4.3b show that electrons and kaons from $\overline{D^0}$, met this requirement, while the same particles in the final state comming from other decays range over a much larger domain of the angles.

Next, invariant mass spectra have been reconstructed for the combination (e^-, K^+) and π^- (e^-, K^+) momenta. The distributions are broad and the center-of-mass energy is shifted with respect to the D^{*-} and $\overline{D^0}$ masses due to the missing momentum of the neutrino. The value of the $\overline{D^0}$ mass stated in [7] is 1.864 GeV. From Fig. 4.4a it is clearly seen that the reconstructed value is significantly smaller than the $\overline{D^0}$ mass. This also holds for the D^{*-} meson, with a mass of 2.010 GeV.

As the D^{*-} decays into a $\overline{D^0}$ and a pion, there should be a correlation between the reconstructed mass of the $\overline{D^0}$ and the momentum of the pion. This correlation is expected to be different from pions not originating from D^{*-} decay. The results from the AROMA Monte Carlo, depicted in Fig 4.5,

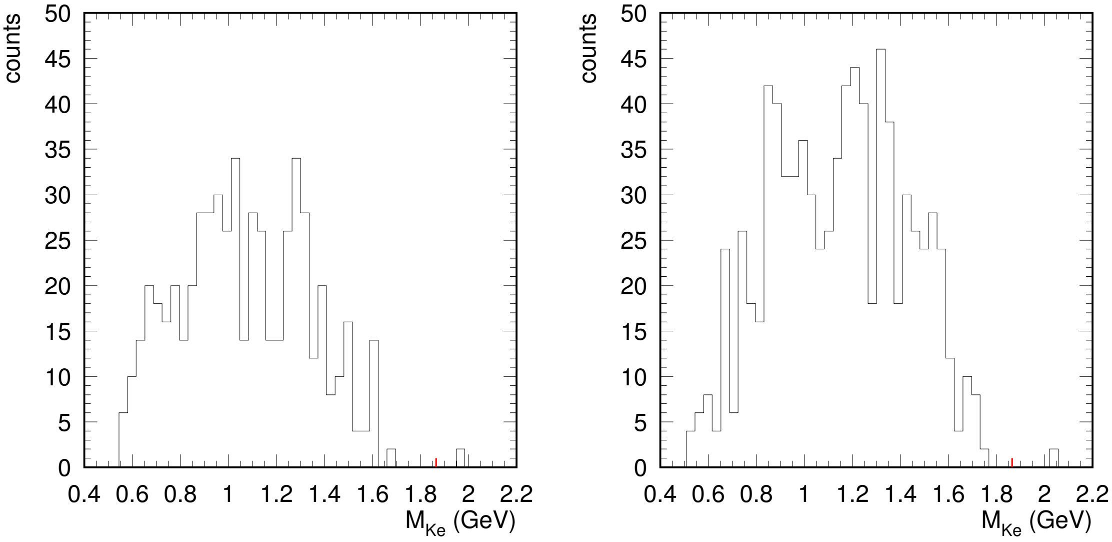

(a) (b)

Figure 4.4: *Invariant mass reconstruction of a* $\overline{D^0}$ *meson. Pion from (a)* $D^{*-} \rightarrow \overline{D^0}\,\pi^-$ *decay and (b) other decay modes (AROMA).*

show that indeed a correlation exists, which can be exploited to distinguish particles from the $D^{*-} \rightarrow \overline{D^0}\pi^-$ decay from those in other D^{*-}decay modes. The decay products from a D^{*-} use a limited region of the phase-space. This region can be approximately described by a circle with the following functional dependence:

$$(p_\pi - 1.2)^2 + (M_{\overline{D^0}} - 1.125)^2 < 0.36\ \mathrm{GeV}^2. \tag{4.4}$$

A further restriction was put forward by selecting only the upper left sector of the circular region, by adding to 4.4:

$$p_\pi < 1.2\ \mathrm{GeV},\ M_{\overline{D^0}} > 1\ \mathrm{GeV}. \tag{4.5}$$

The identification of the D^{*-} from its reconstructed invariant mass is difficult since the reconstruction is partial. This means a broadening of the mass peak, and hence more background in this peak. To improve the resolution of the invariant mass determination a mass-difference (ΔM) of the D^{*-} and

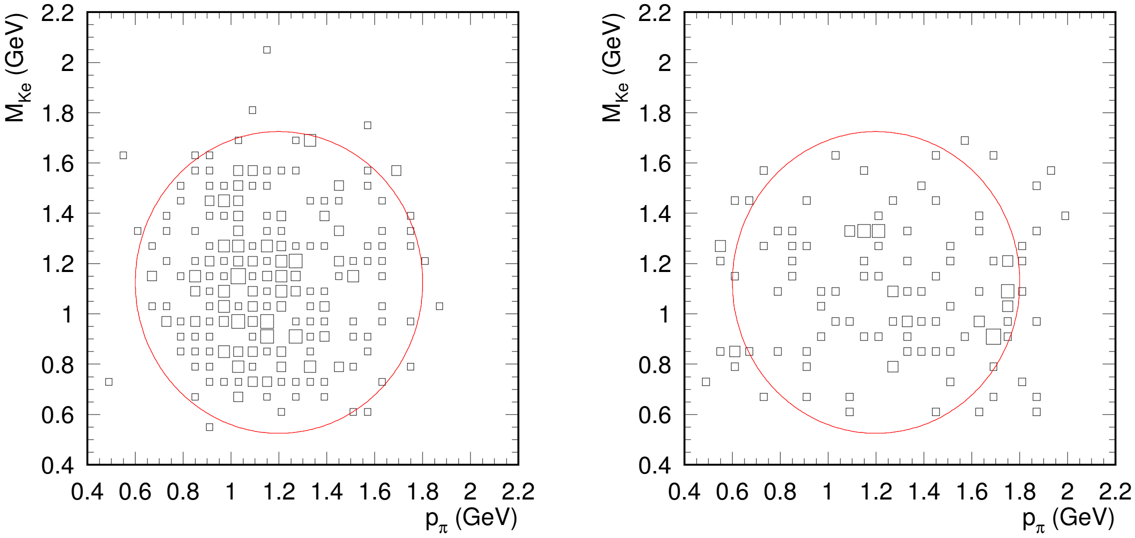

(a) (b)

Figure 4.5: *Reconstructed invariant mass of a* $\overline{D^0}$ *meson versus pion momentum. Pion originating in (a)* $D^{*-} \rightarrow \overline{D^0}\ \pi^-$ *decay and (b) other decay modes (AROMA) containing restrictions 4.1, 4.2, 4.3.*

$\overline{D^0}$ is taken. Assuming that the $\overline{D^0}$ originates from the D^{*-}, the resolution of the peak is improved by cancelling effects due to the non-observation of the neutrino. The final mass-difference spectra are depicted in Fig. 4.6. In this figure it is visible that the mass-difference distribution of the processes in which the pion is not emitted in the decay of the D^{*-}, is much wider than the distribution for the $D^{*-} \rightarrow \overline{D}^0\ \pi^-$ process.

The effects of the restrictions set on the various variables, on the mass-difference spectra for D^{*-} decays are shown in Fig. A.1. Each plot includes one step in optimisation. The same holds for the ΔM for pions not emitted in D^{*-} decay, which has been plotted in Fig. A.2. The data selections increase the ratio of D^{*-} over non-D^{*-} events in the mass difference spectrum drastically. In Table 4.1 the number of events and ratios for D^{*-} and non-D^{*-} events are given.

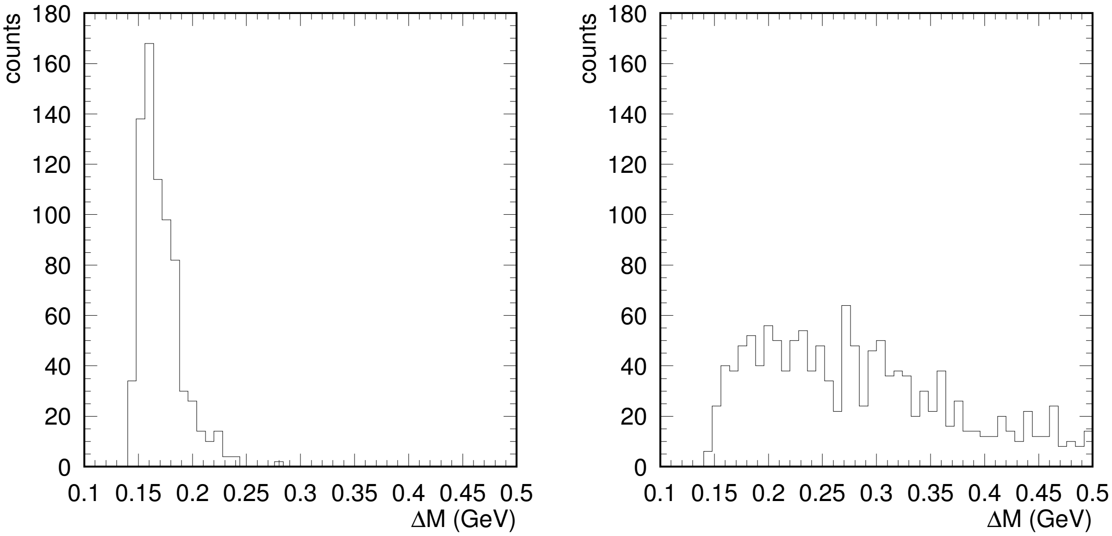

(a) (b)

Figure 4.6: *Difference of reconstructed masses of* π^- $(e^-,\ K^+)$ *and* $(e^-,\ K^+)$. *Pions originating in (a)* $D^{*-} \rightarrow \overline{D^0}\ \pi^-$ *decay and (b) other decay modes, calculated from AROMA.*

Optimisation	D^{*-}	%	non-D^{*-}	%	Ratio
None	738	100%	1474	100%	0.500
Eq. 4.1	684	92%	746	51%	0.917
+ Eq. 4.2	658	89%	708	48%	0.929
+ Eq. 4.3	508	69%	218	15%	2.33
+ Eq. 4.4	482	65%	170	12%	2.83
+ Eq. 4.5	200	27%	58	4%	3.45

Table 4.1: *Number of events in the* ΔM *spectra for* D^{*-} *and non-*D^{*-} *decays and their ratio, for subsequent optimisations, calculated from AROMA.*

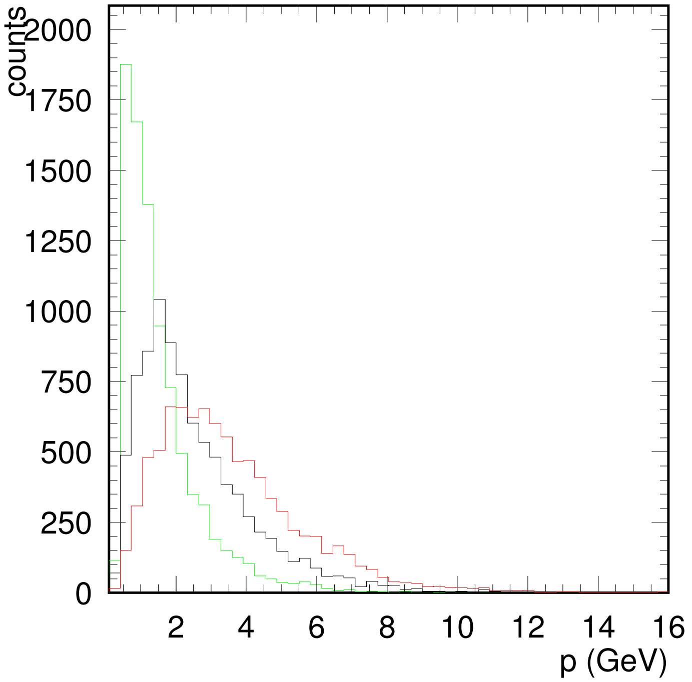

Figure 4.7: *Distribution of pion, electron and kaon momenta originating from non-charmed particles from* PYTHIA.

4.5 Analysis of data obtained from PYTHIA

The momentum distributions of ”non-charmed background” calculated from PYTHIA are compared to those obtained with AROMA in Fig. 4.7. It is clear from this figure why the constraints on the electron momentum were set, ($p_e < 1.5$ GeV). The electron spectrum calculated with PYTHIA shows the largest intensity at small momenta. Hence, this constraint strongly reduces the background in the ΔM spectra. The PYTHIA Monte Carlo has not been normalised to AROMA MC. This means that a quantitative comparison cannot be made. However the shapes of the distributions can be compared.

Fig. 4.8a clearly shows that for a large fraction of the events $p_e + p_K < 4.5$ GeV. Similarly Fig. 4.8b shows that a sizeable fraction of events is beyond the constraints set on the angles of the kaon and electron momenta with respect to the pion momentum. Also a reduction of the $M_{K^+e^-}$ versus p_π phase space reduces the contributions of events from non-charmed particles to the ΔM spectrum. The latter spectrum is presented in Fig. 4.8d. Though all restrictions are included in this spectrum, the width is much larger than in the ΔM spectrum for the process $D^{*-} \to \pi^- \, \overline{D^0} \to \pi^- \, K^+ \, e^-$, indicating that contributions of the latter process to $e^-, \; K^+, \; \pi^-$ events is small.

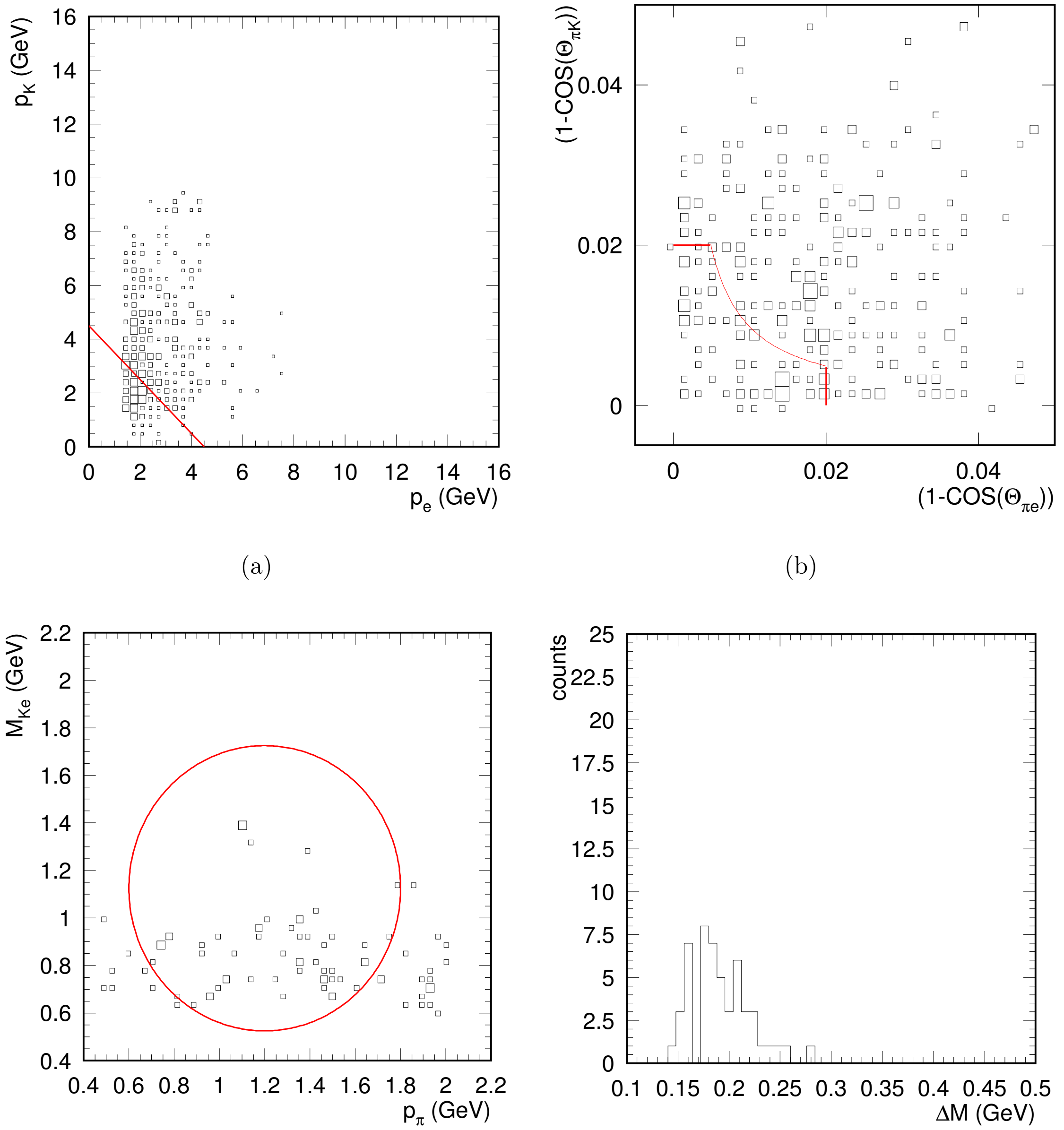

(a) (b)

(c) (d)

Figure 4.8: *Results from calculations performed with* PYTHIA. *(a) Electron versus kaon momentum after restriction 4.1. (b) Angles between π, K and π, e after restrictions 4.1, 4.2. (c) Invariant ”$\overline{D^0}$” reconstructed mass versus π momentum after restrictions 4.1, 4.2, 4.3. (d) Mass difference between $(K\ e\ \pi)$ and $(K\ e)$ after restrictions 4.1, 4.2, 4.3, 4.4.*

5. Conclusions

Monte Carlo simulations with the program AROMA have been performed for the process $D^{*-} \rightarrow \overline{D^0}\pi^- \rightarrow K^+e^-\bar{\nu}_e\pi^-$. and other decay modes of the D^{*-} in which a pion, kaon and electron are emitted. For both sets of Monte Carlo data the phase space spanned by the respective momenta is investigated. By restricting the phase space, and the range in the invariant mass $M(K^+e^-)$ calculated from these momenta, mass-difference spectra, $\Delta M = M(K^+\ e^-\ \pi^-) - M(K^+\ e^-)$, were obtained in which events with $D^{*-} \rightarrow \overline{D^0}\pi^-$ were largely separated from events in which the pion did not originate from the D^{*-} meson. These findings were qualitatively confirmed by calculations performed with PYTHIA. To make a quantitative comparison the results obtained with both programs have to be normalised.

All the restrictions up to 4.4 pass 65% of the $D^{*-} \rightarrow \overline{D^0}\pi^-$ events. This is only 12% for non-D^{*-} events. If restriction 4.5 is taken into account, these values drop to 27% and 4% respectively.

A. Results for ΔM

In this appendix the results of the ΔM spectra extracted from the data obtained from AROMA and PYTHIA are presented. Fig. A.1 shows the results for the decay $D{*}{-} \to \overline{D^0}\pi^- \to K^+ e^- \bar{\nu}_e \pi^-$. Fig. A.2 shows the mass-difference spectra in which the pions originate in other decays. Fig. A.3 shows the PYTHIA results. Calculations given for subsequent restrictions (Eqs. 4.1, 4.2, 4.3, 4.4, 4.5).

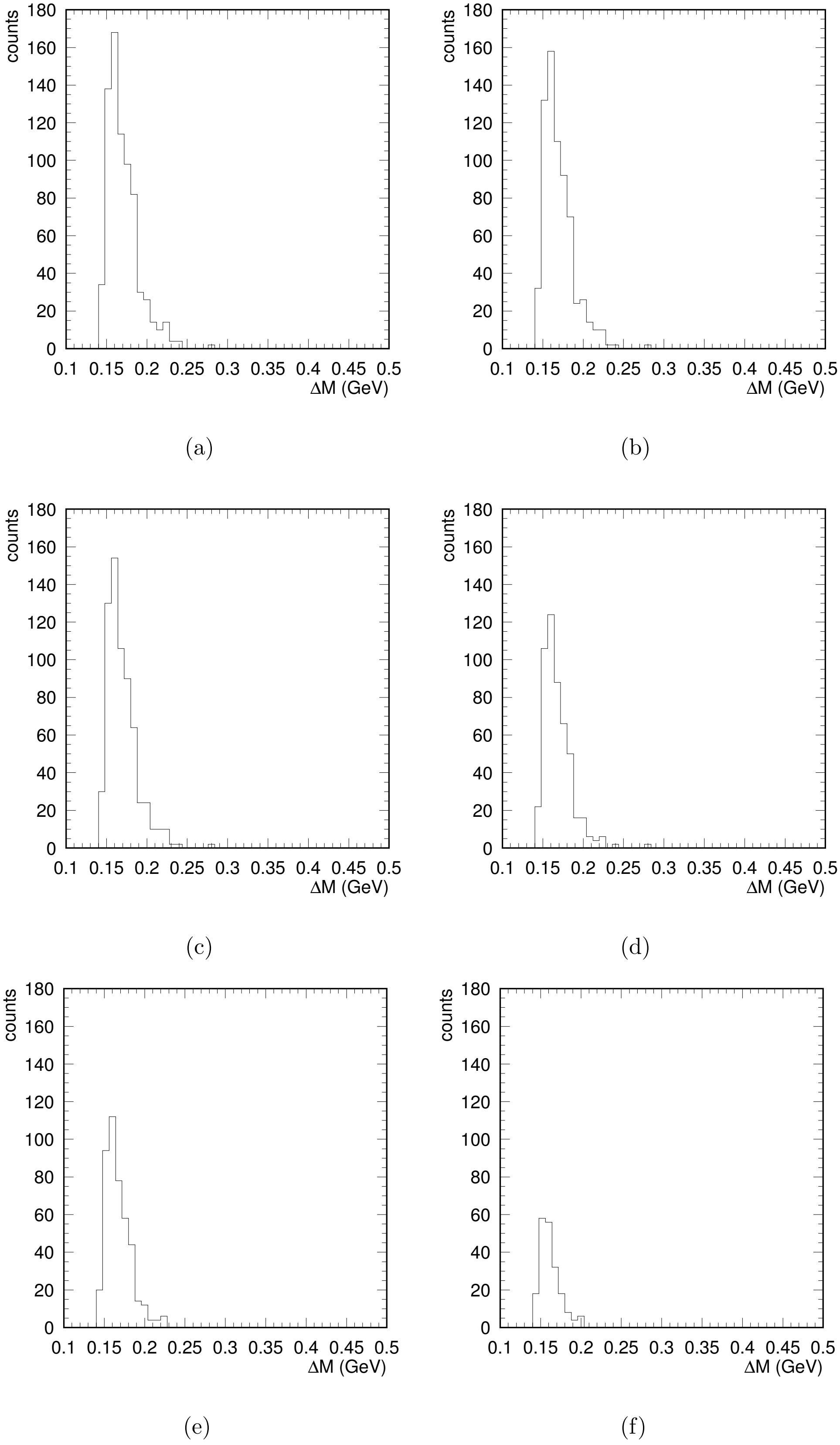

(a) (b) (c) (d) (e) (f)

Figure A.1: *Effects of the restrictions on ΔM for D^{*-} mesons (*AROMA*). (a) No restrictions. (b) Restriction 4.1. (c) Restrictions 4.1, 4.2. (d) Restrictions 4.1, 4.2, 4.3. (e) Restrictions 4.1, 4.2, 4.3 4.4. (f) Restrictions 4.1, 4.2, 4.3, 4.5.*

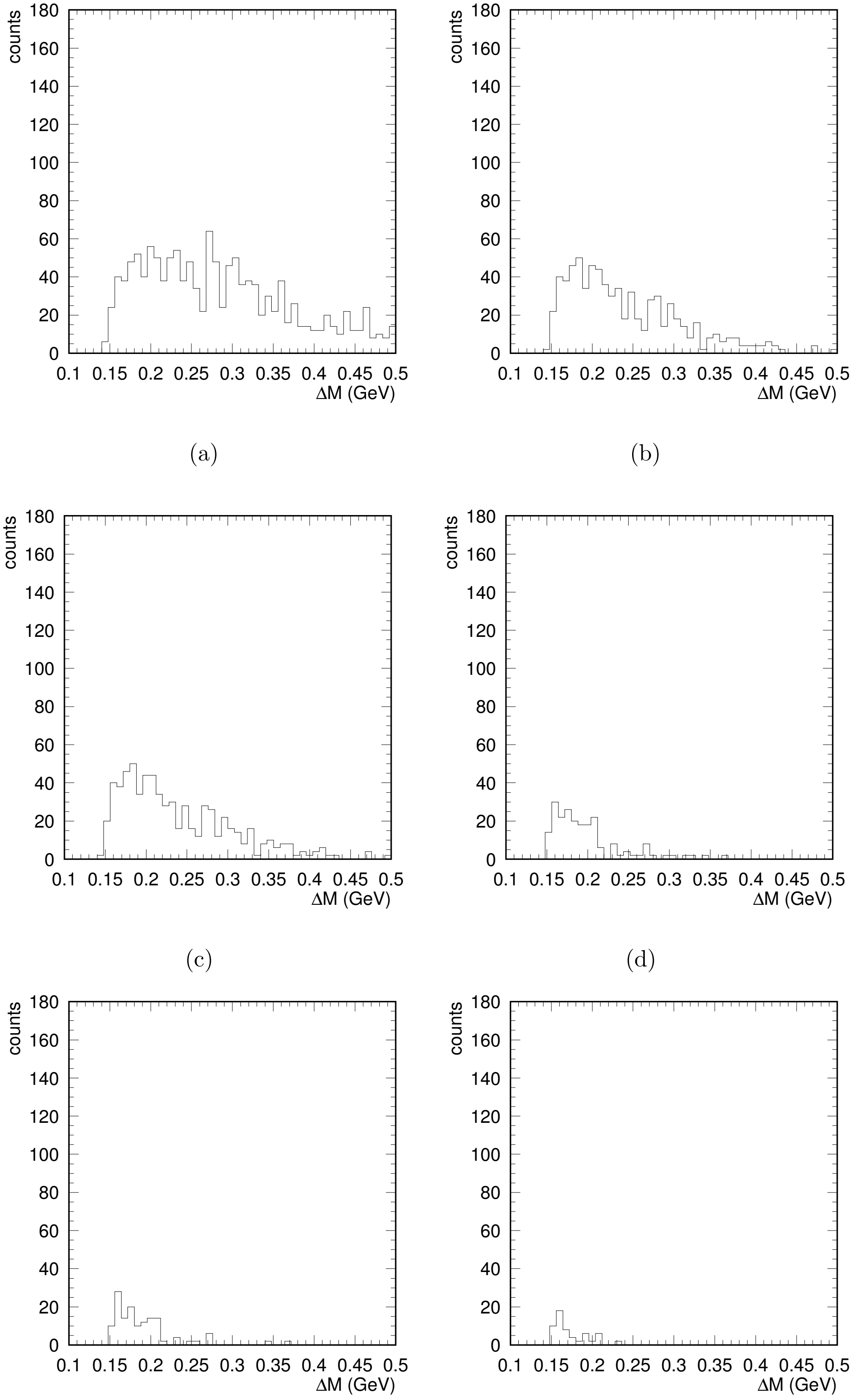

(a) (b)

(c) (d)

(e) (f)

Figure A.2: *Effects of the restrictions on ΔM for non-D^{*-} mesons (AROMA). (a) No restrictions. (b) Restriction 4.1. (c) Restrictions 4.1, 4.2. (d) Restrictions 4.1, 4.2, 4.3. (e) Restrictions 4.1, 4.2, 4.3 4.4. (f) Restrictions 4.1, 4.2, 4.3, 4.5.*

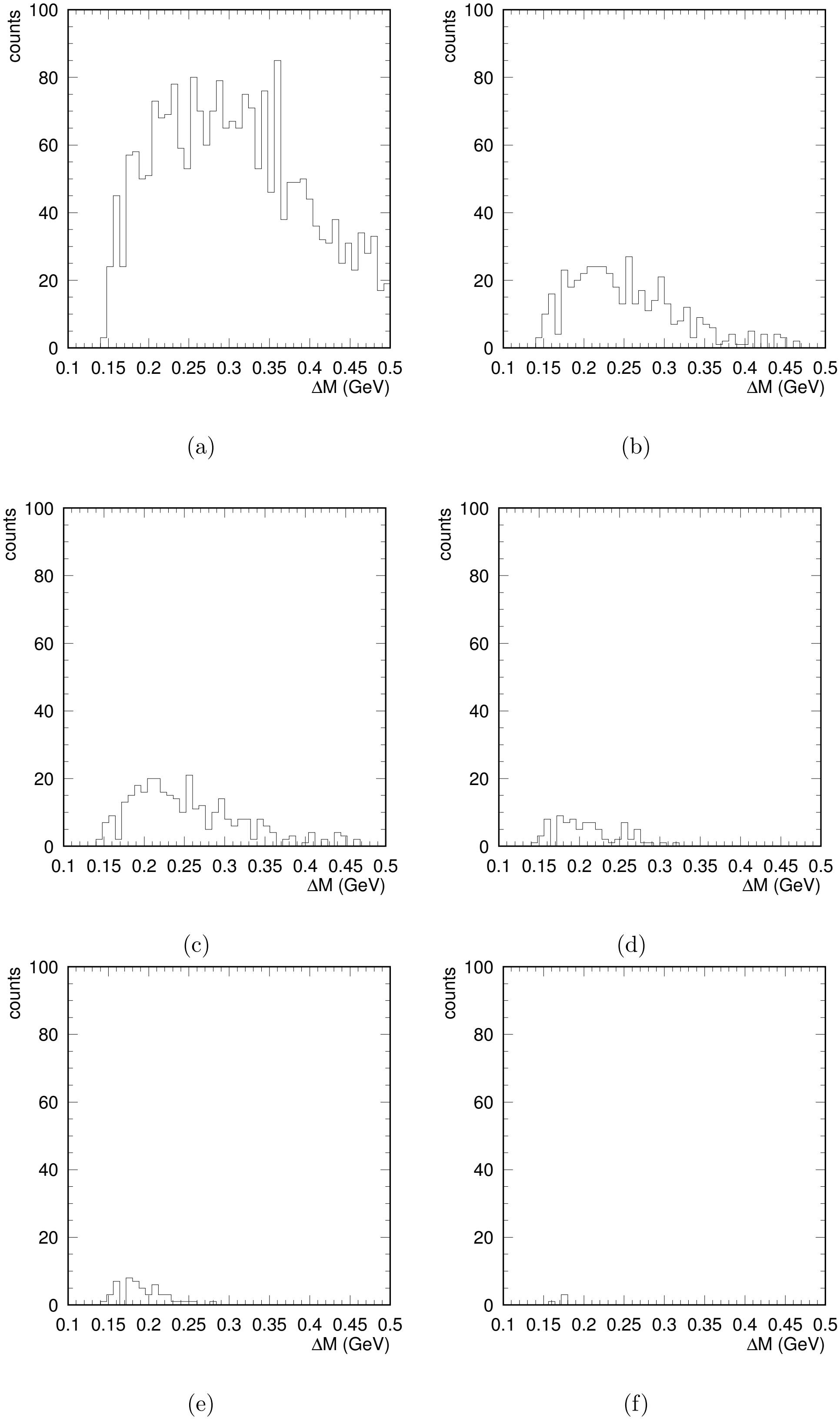

(a) (b) (c) (d) (e) (f)

Figure A.3: *Effects of the restrictions on ΔM for non-charmed mesons (*PYTHIA*). (a) No restrictions. (b) Restriction 4.1. (c) Restrictions 4.1, 4.2. (d) Restrictions 4.1, 4.2, 4.3. (e) Restrictions 4.1, 4.2, 4.3 4.4. (f) Restrictions 4.1, 4.2, 4.3, 4.5.*

References

[1] A. Pais. *The genius of science: A portrait gallery.* Oxford University Press, 2000.

[2] J. Ashman *et al. A measurement of the spin asymmetry and determination of the structure function g_1 in deep-inelastic muon-proton scattering.* Phys. Lett., **B206**, 1988, p. 364.

[3] J. Blouw. *Spin-dependent deep-inelastic positron scattering from polarised He-3.* PhD thesis, Vrije Universiteit Amsterdam, 1998.

[4] M. C. Simani. *Flavor decomposition of the nucleon spin at HERMES.* PhD thesis, Vrije Universiteit Amsterdam, 2002.

[5] F. Halzen and A. D. Martin. *Quarks & Leptons.* John Wiley & sons, 1984.

[6] E. Leader and E. Predazzi. *An introduction to gauge theories and modern particle physics.* Cambridge University Press, 1996.

[7] K. Hagiwara *et al. Review of Particle Physics.* Phys. Rev. D, **66**, 2002, pages 010001+.

[8] B. W. Filippone and X. Ji. *The spin structure of the nucleon.* Note, 2001.

[9] M. Anselmino, A. Efremov, E. Leader. *The theory and phenomenology of polarised deep inelastic scattering.* Phys. Rep., **261**, 1995.

[10] M. P. Alvarez *et al. Study of Charm Photoproduction Mechanisms.* Z. Phys., **C60**, 1993, pages 53–62.

[11] S. J. Brodsky, E. Chudakov, P. Hoyer and J.M. Laget. *Photoproduction of Charm Near Threshold*. Phys. Lett., **B498**, 2001, pages 23–28.

[12] E. Volk. *Measurement of the D^{*-} Cross-section at HERMES*. PhD thesis, Ruprecht-Karls University of Heidelberg, 1999.

[13] H. Wollatz. *Untersuchung von schweren Quarks durch Analyse von Ereignissen mit zwei Myonen am Speicherring HERA*. PhD thesis, University of Hamburg, 1999.

[14] D. Heesbeen. *Quasi-Real Photo-Production of Hyperons on Polarised $^{1,2}H$ Targets*. PhD thesis, Rijksuniversiteit Groningen, 2003.

[15] M. Ehrenfried. *Eine Studie zur Nachweisbarkeit von open charm-Ereignissen bei HERMES*. Master thesis, Westfälische Wilhelms-Universität Münster, 2001.

[16] E. C. Aschenauer, M. Ehrenfried. *Open charm in the 1997 polarised data?* HERMES Internal report, **01-028**, 2001.

[17] P. Bailey, N. C. R. Makins. *Search for the semi-leptonic decay $D^{*-} \rightarrow K^+e^-\pi^-X$*. HERMES Internal report, 2002.

[18] A. Laziev, G. Ybeles Smit, W. Hesselink. *Search for the decay $D^{*-} \rightarrow \overline{D^0}\pi^- \rightarrow \pi^-K^+e^-\bar{\nu_e}$*. HERMES Internal report, 2003.

[19] The HERMES collaboration. *Technical design report*. Technical report, HERMES, 1993.

[20] C. Baumgarten. *Studies of spin relaxation and recombination at the HERMES hydrogen/deuterium gas target*. PhD thesis, Ludwig-Maximilians University of München, 2000.

[21] G. Ingelman *et al.* *LEPTO 6.5 A Monte Carlo Generator for Deep Inelastic Lepton-Nucleon Scattering*. DESY Note, **057**, 1996.

[22] B. Andersson, G. Gustavson, G. Ingelman, T. Sjöstrand. *Parton Fragmentation and String Dynamics*. Phys. Rep., **97 No. 2 & 3**, 1983, pages 31–144.

[23] T. Sjöstrand. *AROMA 2.2*. Computer Physics Commun., **82**, 1994, p. 74.

[24] G. Ingelman *et al. AROMA 2.2 A Monte Carlo Generator for Heavy Flavour Events in ep Collisions*. DESY Note, **058**, 1996.

[25] T. Sjöstrand *et al. PYTHIA 6.2.* Computer Physics Commun., **135**, 2001, p. 238.

[26] T. Sjöstrand *et al. PYTHIA 6.2 Physics and Manual.* DESY note, 2001.

[27] M. Dueren. *HERMES Monte Carlo Workshop.* Workshop Notes, 1994.